ACS OMEGA

http://pubs.acs.org/journal/acsodf

Article

Effective Adsorption of Methyl Orange on Organo-Silica Nanoparticles Functionalized by a Multi-Hydroxyl-Containing Gemini Surfactant: A Joint Experimental and Theoretical Study

Tingting Wang,[⊥] Yaxun Sun,[⊥] Shifeng Wang,* Xin Li, Yihang Yue, and Qi Gao*

Cite This: *ACS Omega* 2021, 6, 18014−18023

Read Online

ACCESS | Metrics & More | Article Recommendations | Supporting Information

ABSTRACT: A novel multi-hydroxyl-containing gemini surfactant (G_{16}) is first designed for modifying silica precursors (SiNPs), with the purpose of fabricating organic adsorbents targeted at methyl orange (MO). The purity of G_{16} and structural character of the resultant G_{16}-SiNPs are unveiled through Fourier transform infrared spectroscopy, X-ray diffraction, thermogravimetry-derivative thermogravimetry, scanning electron microscopy, and surface analysis (BET). Compared with SiNPs, G_{16}-SiNPs exhibit enhanced hydrophobicity, enlarged interlayer spacing, and increased thermal weight losses with the modifier availability reaching as high as 100%. Enhanced MO adsorption is obtained from the higher adsorption capacity of G_{16}-SiNPs (401.88 mg/g) than SiNPs (64.72 mg/g), which is more effective than most of the existing silica-based adsorbents. Pseudo-second-order and Langmuir models conform to all adsorption processes, indicating that the adsorption mainly relies on the availability of adsorption sites and characterized by a homogeneous adsorption form. By combining the experimental study and theoretical calculation methods, it can be demonstrated that the as-synthesized adsorbent G_{16}-SiNPs own multi-active sites that contribute to multi-adsorption mechanisms. The partition process, electrostatic interactions, and OH−π interactions are all responsible for the adsorption performance of G_{16}-SiNPs. This study throws light on the exploration of the superb MO adsorbent in aspects of not only the novel structured modifier and precursor but also theoretical analysis for gaining insights into the adsorption mechanism.

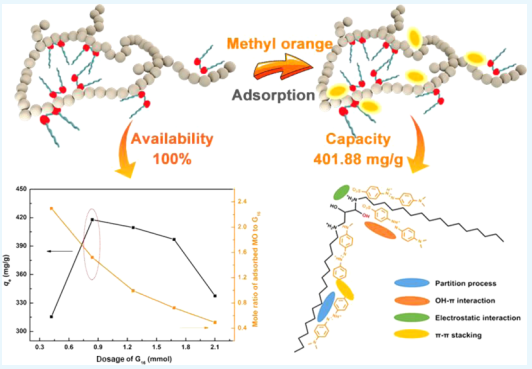

INTRODUCTION

Water pollution has become a big challenge to the global environment and the human race.[1,2] Among the various pollutions to the water environment, dyes used in textiles, chemicals, and other fields pose a threat to the ecosystem that cannot be ignored.[3] Dyes are generally persistent to biodegradation, pyrolysis, and photolysis, posing non-negligible harmful potentialities such as carcinogenicity, mutagenicity, and dysfunction to the human kidney, brain, and liver.[4] Therefore, purification of dye-contaminated wastewater is of great challenge in the contemporary purification technology.[5]

Methyl orange (MO), a typical anionic mono-azo dye, is commonly used in textile and printing industries. Due to the toxic effects of MO degradation intermediates, excessive release of MO results in severe harmful effects. If not properly treated, MO intermediates would remain for a long period of time, leading to potential hazards to the living systems. Numerous purification methods, such as chemical and biological oxidation, photocatalysis, and adsorption, have been explored to deal with MO wastewaters.[6] From the practical perspective, adsorption is recognized as highly selective, facile, and economic in terms of design, operation, and regeneration.[7]

Optimization and enhancement of the adsorbent ability are crucial parts in the adsorption technology. The potentiality of biomass, clays, silicate materials, polymeric and carbonaceous materials, etc., has been extensively exploited for the removal of organic pollutants and dyes.[7,8] Particularly, rigid artificial silica with a controllable structure that can be synthesized simply and quickly (especially 3D silica nanoparticles) emerges as a superb candidate for preparing excellent organic adsorbents.[9,10] The abundant hydroxyl groups and hydrophilic nature within silica nanoparticles, however, limit its affinity and adsorption capacity toward most hydrophobic organic pollutants, which, on the other hand, could be reinforced by specific functionalization routes and/or organic reagents.[11] In the monomeric modifier system, organic modification of the silica precursor (SiNP) has been proven more effective than

Received: April 3, 2021
Accepted: June 30, 2021
Published: July 12, 2021

covalent grafting for the enrichment of smaller dye molecules.[12]

During the whole organic modification and adsorption processes, the modifier structure plays a vital role in aspects of (i) modulating the precursor microstructure, (ii) increasing the precursor hydrophobicity, and (iii) providing additional intermolecular interactions between the adsorbent and targeted adsorbate.[13,14] Gemini surfactants are generally characterized by the linkage of a covalently bonded spacer with two hydrophobic alkyl chains and head groups,[15] whose superiority over the monomeric one has been revealed on bentonite, montmorillonite, and vermiculite in terms of larger interlayer spacing, stronger hydrophobicity, and higher adsorption capacity.[16] The partition process and electrostatic interactions are mainly responsible for the retention of organic pollutants. Notably, adsorption reinforcement could be further achieved through hydrogen bonds, XH$-\pi$ interactions (CH$-\pi$, OH$-\pi$, NH$-\pi$, etc.), $\pi-\pi$ interactions between the aromatic rings, and interactions between the aromatic ring and heteroaromatic ring.[17−19] The introduction of the hydroxyl group into the modifier structure provides not only hydrogen bonds but also non-negligible OH$-\pi$ interactions, which have been proven effective for the retention of sulfamethoxazole (SMX) and phenols. Moreover, the number of hydroxyl groups in the modifier is positively correlated with the capacity, application effect, and loading capacity of the adsorbent.[20]

Notably, theoretical simulation methods are powerful tools for understanding the mechanism in various adsorption systems.[21] Insights have been gained from frontier molecular orbitals, adsorption isosteric heat, and bond lengths.[22] Possible active sites and intermolecular interactions could be predicted by the highest occupied molecular orbital (HOMO) and the lowest unoccupied molecular orbital (LUMO) through accepting or donating electrons based on density functional theory (DFT),[23] which have been successfully applied to analyze interactions between organo-SiNPs and tritoluene dyes (malachite green, crystal violet, and bromophenol blue).[12] To date, theoretical investigations about the modification of organo-SiNPs are limited at hexadecyl trimethyl ammonium bromide and hexadecyl trimethoxysilane, which are seldomly extended to the modification and simulation about organic modification of SiNPs by functional gemini surfactants.[12]

To explore the potentiality of the SiNP-based adsorbent, to enrich the existing modifier species, and to pursue the novel adsorbent with prominent properties, a multi-hydroxyl-containing gemini surfactant (G_{16}) is first adopted to functionalize SiNPs for preparing organic adsorbents toward MO. The structural property, thermostability, modifier arrangement, and availability of the resultant G_{16}-SiNPs are revealed through a series of probing techniques. The influencing factors of the adsorption process were explored. On this basis, the kinetic and thermodynamic properties of the adsorption process were obtained, and the adsorption mechanism was clarified. The relationships between G_{16}-SiNPs and MO are elucidated not only by geometry optimization but also by frontier molecular orbitals by DFT. Finally, considering the recyclability of the adsorbent, research studies on recovery and regeneration were carried out. The results in this study not only present a detailed and systematic view of a superb MO adsorbent but also provide guidelines for designing novel silica-based adsorbents and throwing light on multi-hydroxyl groups for adsorption enhancement.

2. EXPERIMENTAL SECTION

2.1. Materials. $Na_2SiO_3{\cdot}9H_2O$ is provided by Sigma-Aldrich. The raw materials for synthesizing G_{16}, *N*,*N*-dimethylhexadecylammonium (DHA), and 1,4-dibromo-2,3-butanediol (DBBD) are obtained from Sigma-Aldrich. HNO_3, ether, ethanol, and *n*-propanol are supplied by Beijing Chemical Works. The pH-adjusted reagents HCl and NaOH are supplied by Beijing Chemical Works. MO is obtained from J&K Scientific Ltd. All chemicals are of analytical grade and used without further purification.

2.2. Experimental Procedures. G_{16} is synthesized as follows: certain amounts of DHA (17.6 mmol, excess 20%) dissolved in 35 mL of *n*-propanol are placed in a 100 mL round-bottomed flask. After adding 7.33 mmol of DBBD dropwise, the mixture is stirred at 95 °C for 64 h. The raw products are obtained by vacuum evaporation and recrystallization from ether/ethanol mixtures. The purity of G_{16} is examined by the melting point (mp), elemental analysis (EA), and Fourier transform infrared spectroscopy (FT-IR).

The synthesis procedure of SiNPs is to dissolve 6.5 g of $Na_2SiO_3{\cdot}9H_2O$ in deionized water (the molar ratio of H_2O to Na_2SiO_3 is 60:1). Subsequently, 3 mol/L of HNO_3 is added dropwise into the mixture under vigorous stirring until the pH reaches 7 under 30 °C. Then, the mixture is aged at 60 °C for 20 h. The final product is obtained by washing with deionized water, centrifuging five times, and drying at 100 °C overnight. The cationic exchange capacity (CEC) of SiNPs is 42 mmol/100 g.[2]

G_{16}-SiNPs are prepared as follows: after separately dissolving certain amounts of G_{16} (0.42, 0.84, 1.26, 1.68, and 2.10 mmol, corresponding to 1, 2, 3, 4, and 5 CEC of SiNPs, respectively) and 1 g of SiNPs in deionized water (40 and 10 mL, respectively), the solution is stirred for 1 h under 70 °C. Organic modification is proceeded by mixing G_{16} and SiNP solutions and reacting the mixture under 70 °C for 3 h. The final products are obtained by centrifuging, washing, and drying overnight.

2.3. Characterization. Fourier transform infrared (FT-IR) spectroscopy (MO, G_{16}, SiNPs, G_{16}-SiNPs, and adsorbed G_{16}-SiNPs), X-ray diffraction (XRD; XRD patterns of SiNPs and G_{16}-SiNPs), thermogravimetric analysis [thermogravimetry-derivative TG (TG-DTG) curves of G_{16}, SiNPs, and G_{16}-SiNPs], EA (EA of G_{16}, SiNPs, and G_{16}-SiNPs), and scanning electron microscopy (SEM; SEM images of SiNPs and G_{16}-SiNPs) are conducted to characterize the structural properties. The values of zeta potential of G_{16}-SiNPs are recorded by immersing 0.03 g of G_{16}-SiNPs in water solutions at pH of 3, 5, 7, and 9. Specific operating parameters are presented in the Supporting Information.

2.4. Adsorption Experiment. Batch adsorption experiments are adopted for evaluation of the adsorbent performance and clarification of the adsorption mechanism. Analysis about the adsorption mechanisms (such as kinetics, isotherms, and thermodynamics) is conducted by mixing G_{16}-SiNPs and MO solution under varying time intervals, MO concentrations, and temperatures, respectively. The effect of pH on adsorption is conducted at the values of 3, 5, 7, and 9. The adsorption experiments are performed using the batch equilibration technique. 0.03 g of G_{16}-SiNPs is dispersed into 30 mL of MO solution in a 50 mL conical flask (with a sealed cap). Also, the mixtures are shaken at a speed of 200 rpm in a constant temperature water bath for 3 h. After centrifugation, the

https://doi.org/10.1021/acsomega.1c01788
ACS Omega 2021, 6, 18014−18023

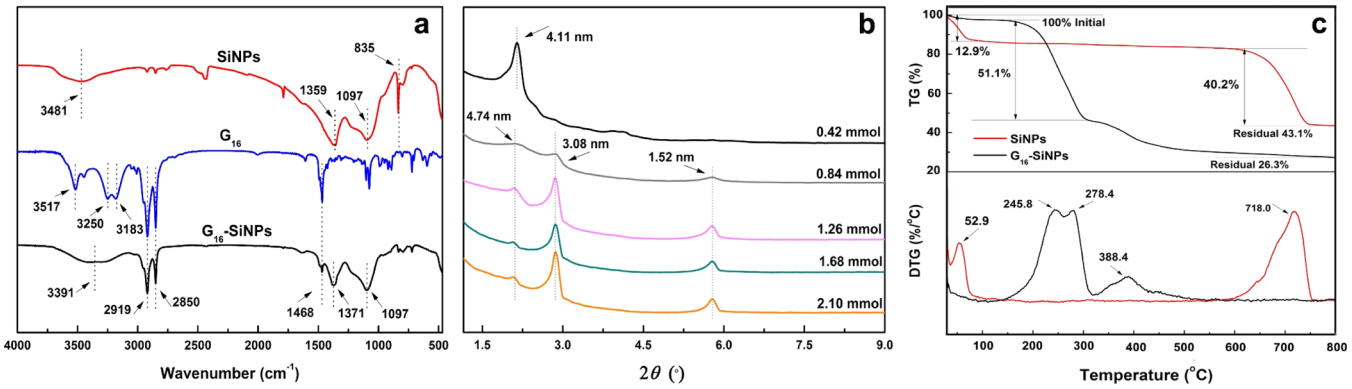

Figure 1. FT-IR spectra (a), XRD patterns (b), and TG-DTG curves (c) of G_{16}, SiNPs, and G_{16}-SiNPs.

supernatant is analyzed with a UV-2550 spectrophotometer at 464 nm at a pH of 7. The concentration of MO is calculated by the standard curve equation. The adsorption capacity of G_{16}-SiNPs toward MO is obtained by the following equation:

$$q_e = \frac{C_0 - C_e}{m} V \quad (1)$$

where q_e (mg/g) is the adsorption capacity of G_{16}-SiNPs and C_0 and C_e (mg/L) are the initial and equilibrium concentrations of MO solution, respectively. m (g) is the mass of the adsorbent and V (L) is the volume of MO solution.

The regeneration experiment is conducted by immersing 1 g of the spent adsorbent in 50 mL of ethanol and stirring for 3 h under room temperature. Conditions of the re-adsorption are the same as those of adsorption experiments.

2.5. Theoretical Calculations. All the quantum chemical calculations are performed by using Material Studio 8.0. The calculation of the frontier orbitals and optimized structures of molecules is based on the DFT. Calculations are conducted using the Dmol3 module, in which the process using the function GGA&BLYP (generalized gradient approximation and Becke−Lee−Yang−Parr) is used. To obtain the optimized adsorbent−adsorbate structure, the Adsorption Locator module is used, and the force field is set to universal.

3. RESULTS AND DISCUSSION

3.1. Characterization of G_{16}. The FT-IR spectra of G_{16} are shown in Figure 1a. Peaks at 2919 and 2850 cm^{-1} are associated with the stretching vibrations of the alkyl chain within G_{16}, whose bending vibration is characterized by the peak at 1468 cm^{-1}. Peaks around 3250 (3183) and 3517 cm^{-1} are resulted from the OH groups (two OH groups with different conformations) and water molecules within the G_{16} structure.

EA results of G_{16}: calculated value: C 63.80%, H 10.89%, N 4.30%. Test value: C 64.21%, H 10.06%, N 4.82%. The mp of G_{16} is measured to be 196.3−197.0 °C. Combining the results from FT-IR, EA, and mp, it can be concluded that G_{16} is the target product with a high purity.

3.2. Characterization of G_{16}-SiNPs. *3.2.1. FT-IR Analysis.* The FT-IR spectra of SiNPs and G_{16}-SiNPs are depicted in Figure 1a. In the spectrum of SiNPs, the anti-symmetric and symmetric stretching vibrations of Si−O bonds are observed at 1097 and 835 cm^{-1}, respectively, representing the existence of the Si−O framework.[24,25] The peak at 1359 cm^{-1} is related to the N═O stretching vibrations derived from HNO_3 (i.e., the solvent for synthesizing SiNPs),[26] indicating the existence of interactions between N═O (i.e., NO_3^-) and the surface of SiNPs, which is consistent with the considerable N content in SiNPs (Table 1). Moreover, due to the negative charge of NO_3^-, its existence on the SiNP surface may be responsible for the CEC of SiNPs, offering considerable active sites for the combination of the cationic modifier G_{16}.[12]

Table 1. Elemental Analysis Results (wt %) of SiNPs, G_{16}, and G_{16}-SiNPs.

sample	C	H	N
SiNPs	0.12	2.32	2.73
G_{16}	64.21	10.06	4.82
G_{16}-SiNPs	40.22	6.94	5.66

The spectrum of G_{16}-SiNPs exhibits combined characteristic peaks of G_{16} and SiNPs, supporting the successful modification process. As shown in the FT-IR spectra of G_{16}-SiNPs, peaks at 2919, 2850, and 1468 cm^{-1} indicate the incorporation of the alkyl chain into the structure of G_{16}-SiNPs. Compared with the raw SiNPs, the shift of the OH-associated peak (from 3481 to 3391 cm^{-1}) and the structural Si−OH peak (from 1359 to 1468 cm^{-1}) in G_{16}-SiNPs indicate the hydrophobicity variation due to the intercalation of G_{16}.[27] Moreover, variation in the location and strength of the N═O peak in G_{16}-SiNPs compared with SiNPs (from 1359 to 1371 cm^{-1}) indicates the participation of NO_3^- for bonding with G_{16} in the modification process.

3.2.2. XRD Analysis. SiNPs were present as an agglomerated morphology with silica particles orderly connecting to each other.[2] After incorporation with G_{16}, intermolecular interactions between adjacent modifiers on different precursor surfaces would further facilitate the aggregation into a staked whole, thus leading to the expansion of interlayer space and emergence of interlayer spacing in the XRD patterns of G_{16}-SiNPs (Figure 1b).

Modifier arrangement within SiNPs could be deduced from the combined information of the G_{16} molecular size and interlayer spacing of G_{16}-SiNPs.[28] The lengths of the alkyl chain and the spacer and the height of G_{16} are approximately 1.98, 0.63, and 0.31 nm, respectively. As seen from Figure 1b, the interlayer spacing of G_{16}-SiNPs increases from 4.11 nm (0.42 mmol) to 4.74, 3.08, and 1.52 nm (0.84−2.10 mmol). It can be deduced that the arrangement of G_{16} is evolved from the paraffin-bilayer arrangement to the coexistence of the pseudotrimolecular layer, paraffin bilayer, and lateral bilayer arrangements. The more the modifier dosage, the greater the

https://doi.org/10.1021/acsomega.1c01788
ACS Omega 2021, 6, 18014−18023

diversity of modifier molecules arranged within the interlayer space of SiNPs. The XRD patterns of G_{16}-SiNPs remain constant at the modifier dosage of 0.84 mmol, suggesting the saturated quantity of G_{16} on SiNPs.

3.2.3. TG-DTG Analysis and EA Results. TG-DTG analysis is adopted to verify the hydrophobic variation during the modification process and to estimate the thermostability of the resultant G_{16}-SiNPs. The TG-DTG curves of SiNPs and G_{16}-SiNPs are shown in Figure 1c, and the TG-DTG curves of G_{16} are depicted in Figure S1.

As shown in Figure S1, a sharp weight loss of G_{16} is observed at around 305.8 °C, indicating that the decomposition of G_{16} starts at as high as 300 °C. Compared with the weight losses in Figure 1c, organic functionalization decreases the thermostability of G_{16}, which may be due to the involvement of interactions between the organic modifier and SiNPs. The intercalation manner of G_{16} into SiNPs and the thermostability of G_{16}-SiNPs are evaluated by TG-DTG curves (Figure 1c). Two distinct weight loss stages are observed in the raw SiNPs (52.9 and 718.0 °C), which mean the desorption of physically adsorbed water molecules and dihydroxylation of Si−OH units, respectively.[29] With the increase of temperature, the hydroxyl groups start to get removed after the loss of physically adsorbed water molecules.[30] At the temperature of around 700−1000 °C, almost all the silica surface would condense into the siloxane condition. In the dehydroxylation stage, the removal of one water molecule means that two hydroxyl groups are reduced.[31] The existence of enormous structural Si−OH is validated by considerable weight losses around 718 °C (nearly 40.2%).

Compared with SiNPs, disappeared peaks at 52.9 and 718.0 °C verify (i) the increased hydrophobicity of G_{16}-SiNPs due to organic modification and (ii) the important role of Si− OH in the organic modification process. Interactions between the hydroxyl groups in G_{16} and the structural Si−OH in SiNPs would affect the stability of Si−OH, leading to the disappeared dehydroxylation process in G_{16}-SiNPs. The loss of G_{16} in SiNPs is not a simple desorption procedure but also involves a complicated decomposition process, where the surfactants would decompose into small organic molecules with the increase of temperature.[32] In this study, interactions between G_{16} and the structural Si−OH may lead to the advanced loss of hydrogen atoms, which impedes the dehydroxylation process with the increase of temperature.

Moreover, additional weight losses between 200 and 500 °C in G_{16}-SiNPs are resulted from the organic modifier. Organic modification is mainly achieved through electrostatic interactions (between the N^+ head group in G_{16} and NO_3^- in SiNPs), physical adsorption (between the OH in G_{16} and Si−OH in SiNPs), and van der Waals forces (between the alkyl chains in G_{16}).[33] The strengths of binding from the corresponding temperatures of three weight loss stages are as follows: electrostatic interactions (388.4 °C) > physical adsorption (278.4 °C) > van der Waals forces (245.8 °C).

As shown in Table 1, the actual modifier loading could be calculated from the higher carbon content in G_{16}-SiNPs (40.22%) than SiNPs (0.12%). Given the actual carbon percentage of G_{16}, the amount of the modifier loaded is calculated to be 52.63% on G_{16}-SiNPs, which is nearly consistent with the first two weight losses in TG-DTG (51.1%), indicating that G_{16} molecules are bonded mainly through physical adsorption and van der Waals forces. Notably, the modifier availability (ratio of modifier molecules loaded to added) of G_{16} on SiNPs reaches nearly 100%, demonstrating the great potentiality and promising aspect of SiNPs for submitting organic modification processes.

3.2.4. SEM Images and BET Analysis. The SEM image and BET surface area of SiNPs and G_{16}-SiNPs are measured and shown in Figure 2. SiNPs exhibit an unordered morphology

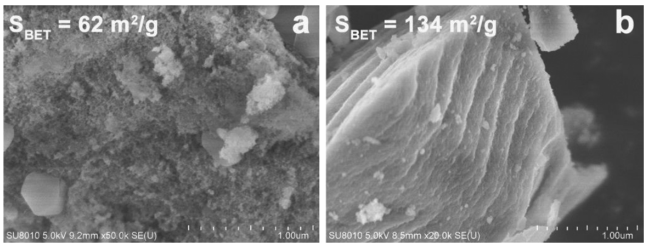

Figure 2. SEM images of SiNPs (a) and G_{16}-SiNPs (b).

with silica nanoparticles stacking irregularly on the incompact surface. After organic modification, the surface of G_{16}-SiNPs is denser. Interactions (van der Waals forces and hydrogen bonds) between G_{16} molecules on different surfaces could aggregate the particles of G_{16}-SiNPs into a stacked whole, thus leading to the aggregation of neighboring G_{16}-SiNPs into a large and irregular shape.[20]

SiNPs and G_{16}-SiNPs exhibit the surface areas of 62 and 134 m^2/g, respectively. In the relative high P/P_0 region, the adsorption/desorption branches of SiNPs and G_{16}-SiNPs have a slight adsorption hysteresis, which manifest that the curves are in accordance with a type IV isotherm with type H1 (Figure S2). The BET-N_2 surface area and the total pore volume (Table S1) of G_{16}-SiNPs exhibit a slight decrease over the pristine one, which may be due to the coverage of the precursor surface by the long alkyl chains of G_{16}, which hinder the approach of nitrogen to G_{16}-SiNPs.

3.3. Adsorption Tests. *3.3.1. Effect of G_{16} Dosage on Adsorption.* Variation of MO adsorption with the modifier dosage is depicted in Figure 3 (the initial MO concentration is 500 mg/L). As shown in Figure 3, MO adsorption amounts are greatly improved after the functionalization of G_{16} on SiNPs (approximately 300−420 mg/g compared with the adsorption capacity of the raw SiNPs of 64.72 mg/g), indicating the great improvement of G_{16} for MO adsorption.

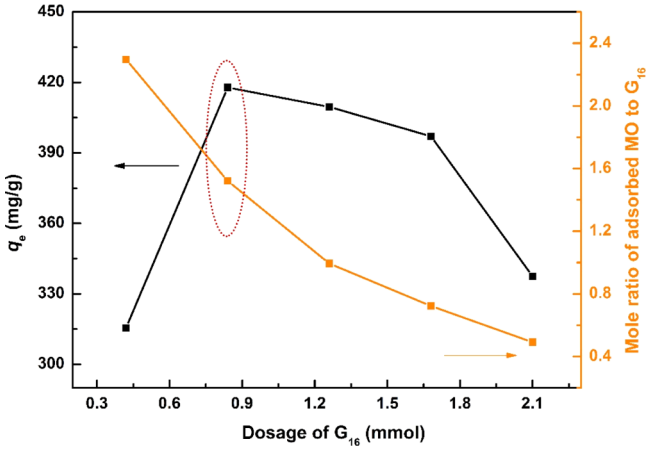

Figure 3. Effect of modifier dosage on the adsorption of MO onto G_{16}-SiNPs.

https://doi.org/10.1021/acsomega.1c01788
ACS Omega 2021, 6, 18014−18023

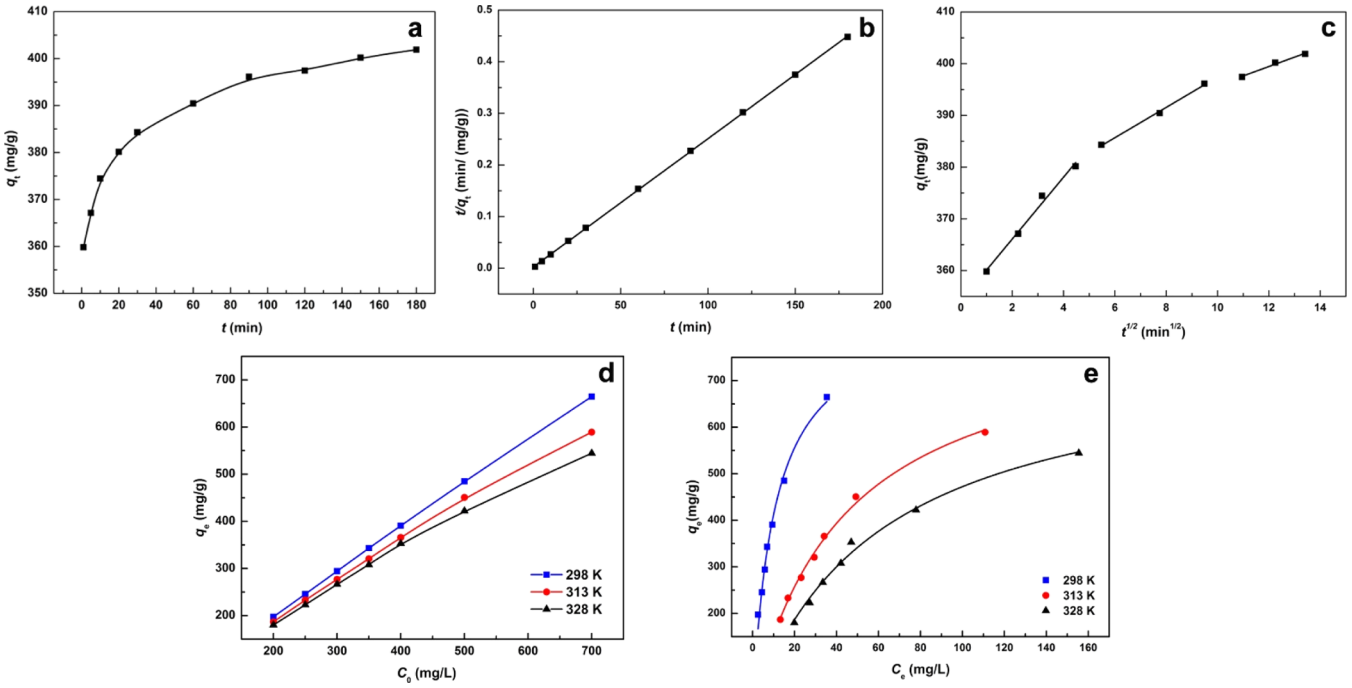

Figure 4. Effects of time (a), MO concentration (d), pseudo-second order (b), intra-particle diffusion (c), and Langmuir isotherm (e) on the adsorption of MO onto G_{16}-SiNPs.

Table 2. Kinetic Parameters for the Adsorption of MO onto G_{16}-SiNPs[a]

		pseudo-first order				pseudo-second order					intra-particle diffusion			
adsorbents	$q_{e,exp}$	$q_{e,cal}$	k_1 (10^{-2})	R^2	SSE (10^{-4})	$q_{e,cal}$	k_2 (10^{-2})	k_2q_e	R^2	SSE (10^{-4})	k_{id}	C (10^2)	R^2	SSE
G_{16}-SiNPs	401.88	44.79	2.5	0.8815	3.01	401.61	0.249	1.51	0.9999	0.19	2.93	3.68	0.9941	0.21

[a] $q_{e,exp}$ (mg g^{-1}), $q_{e,cal}$ (mg g^{-1}), k_1 (min^{-1}), k_2 (g mg^{-1} min^{-1}), k_{id} (mg g^{-1} $min^{1/2}$), C (mg g^{-1}).

In terms of G_{16}-SiNPs, MO adsorption keeps increasing, followed by gradual decrements with G_{16} feeding. These trends could be explained as follows: on one hand, the inserted G_{16} enhances the hydrophobicity of the alkyl chain and at the same time generates hydrogen bonds and OH−π interactions. This series of interactions produces a large number of activation points on the adsorbent surface that can be used for adsorption, which promotes the upward trend of adsorption.[34] On the other hand, excess G_{16} molecules would result in severe blocking of the adsorbent gallery and porosity, which impedes the adsorption process for a further degree.[35]

Given the adsorption capacity and mole ratio of MO to G_{16}, 0.84 mmol is set as the saturated modifier dosage in the subsequent adsorption experiments, which is consistent with XRD results.

3.3.2. Effect of Time and Adsorption Kinetics. A slow adsorption equilibrium is observed with prolonged time (Figure 4a), and the required equilibrium time is approximately 120 min. To further clarify the kinetic characters, pseudo-first-order, pseudo-second-order, and intra-particle diffusion models are adopted to fit the adsorption data (Table 2).

The equations of pseudo-first-order (2), pseudo-second order (3), and intra-particle diffusion (4) models are expressed as follows:[20]

$$\log(q_e - q_t) = \log q_e - \frac{k_1}{2.303}t \quad (2)$$

$$\frac{t}{q_t} = \frac{1}{k_2 q_e^{\,2}} + \frac{1}{q_e}t \quad (3)$$

$$q_t = k_i t^{1/2} + C \quad (4)$$

where k_1 (min^{-1}) and k_2 (g (mg $min)^{-1}$) are the rate constants. q_e (mg g^{-1}) and q_t (mg g^{-1}) stand for the adsorption capacities at equilibrium and at time t (min), respectively. All these unknown parameters can be determined from plots of $\ln(q_e - q_t)$ against t and t/q_t against t. k_{id} (mg g^{-1} $min^{-1/2}$) is the rate constant of the intra-particle diffusion, and the values of C and k_{id} can be determined from the intercept and slope of the linear plot of q_t against $t^{1/2}$, respectively.

The pseudo-second-order model (Figure 4b and Table 2) provides the best correlation for the adsorption process with a higher correlation coefficient (the value of R^2 is 0.9999), a lower SSE value (0.19), and greater consistency of $q_{e,cal}$ to $q_{e,exp}$ (401.61 to 401.88 mg/g), suggesting that the adsorption processes may be mainly affected by chemical adsorption.

Moreover, three sections during the adsorption process could be observed from the intra-particle diffusion model (Figure 4c).[36] The high concentration of MO solution diffuses to the adsorbent surface rapidly, gradually occupying the active binding sites on the adsorbent surface and weakening the driving force by concentration gradient between MO solution and the adsorbent surface. The gradual diffusion of MO into G_{16}-SiNPs could account for the slowing down of the second stage in the intra-particle diffusion model. The adsorption

https://doi.org/10.1021/acsomega.1c01788
ACS Omega 2021, 6, 18014−18023

Table 3. Adsorption Isotherm Constants for the Adsorption of MO onto G_{16}-SiNPs[a]

	Langmuir			Freundlich			Redlich Peterson			
temperature	q_{max}	K_L	R^2	K_f	n	R^2	a	b	g	R^2
298 K	852.2	0.093	0.9988	73.47	3.15	0.9754	120.67	0.33	0.78	0.9943
313 K	834.3	0.022	0.9964	61.74	2.06	0.9625	16.61	0.01	1.13	0.9958
328 K	764.4	0.016	0.9909	49.78	2.08	0.9570	10.95	0.01	1.14	0.9905

[a] q_{max} (mg g^{-1}), K_a (L mg^{-1}), K_f (mg g^{-1}), a (L g^{-1}), b (J mol^{-1}).

capacity attains the final equilibrium in third stage.[37] Intraparticle diffusion is not the only reason that affects the rate. The adsorption rate is controlled by multiple processes, which is supported by the fact that all the lines do not pass through the origin (Figure 4c).

3.3.3. Concentration of MO and Isotherms. To unveil the adsorptive effect of G_{16}-SiNPs, one of the UV−vis spectra of neat MO solution before and after adsorption is measured and presented in Figure S3. Considering the measuring range of UV−vis, an initial MO concentration of 100 mg/L is chosen in the measurement of UV−vis spectra. As shown in Figure S3, the wide and strong characteristic peak of the spiked MO sample is greatly weakened after treatment by G_{16}-SiNPs, indicating the effective removal performance of G_{16}-SiNPs. Meanwhile, the color difference between MO solution before and after adsorption reveals the obvious adsorptive effect of G_{16}-SiNPs from a visual perspective. This result further confirms that G_{16}-SiNPs are a kind of efficient adsorbent for MO.

The relationship between the MO concentration and the amount of adsorption is given in Figure 4d. It can be clearly seen that as the MO concentration increases, the amount of adsorption increases too. The great concentration difference between MO solution and the surface of the adsorbent enhances the driving force of adsorption and other interactions (such as OH−π interactions between G_{16}-SiNPs and MO or π−π stacking between MO molecules). The highest adsorption amounts of MO could reach as high as 665 mg/g under the tested conditions (298 K with the initial MO concentration of 700 mg/L).

The Langmuir, Freundlich, and Redlich−Peterson isotherms are expressed as follows:[20]

$$q_e = \frac{Q_m K_L C_e}{1 + K_L C_e} \quad (5)$$

$$q_e = K_f C_e^{1/n} \quad (6)$$

$$q_e = \frac{A C_e}{1 + B C_e^{g}} \quad (7)$$

where q_e (mg/g) is the adsorption capacity onto per unit mass of the adsorbent at equilibrium, C_e is the solute equilibrium concentration (mg/L), and q_m (mg/g) is the maximum theoretical adsorbed amount. k_L (L/mg), k_f (mg/g), and n represent the constants of Langmuir and Freundlich, respectively. A (L/g) and B ($(L/mg)^g$) are the Redlich−Peterson model constants. g fluctuates between 0 and 1.

Compared with the linear formed Langmuir isotherms, the nonlinear Langmuir model (Figure 4e) has been demonstrated to be the most accurate for representing the experimental data.[38] The nonlinear equilibrium isotherms are summarized in Table 3. The correlation coefficients R^2 calculated by the Langmuir model at all tested temperatures are all greater than 0.99, which means a better fitting than the Freundlich model, suggesting that MO molecules are captured by specific sites within G_{16}-SiNPs and arranged in a monolayer form. Due to the high modifier availability, G_{16}-SiNPs could offer abundant active sites for MO adsorption. From the isotherm results, it can be deduced that MO is mainly immobilized and interacts with G_{16} through hydrophobic and OH−π interactions, which is characterized by monolayer arrangement. Higher affinity between G_{16} and MO than that between adsorbed MO and dissolved MO molecules weakens the secondary interactions (i.e., π−π stacking),[39] leading to the preferable monolayer arrangement, as fitted by the Langmuir isotherm.

The maximum adsorption capacities (q_{max}) calculated by the Langmuir isotherm are 852.2, 834.3, and 764.4 mg/g under 298, 313, and 328 K, respectively, which are higher than those of most of the MO adsorbents reported recently (Table 4).[40−46]

Table 4. Comparison of MO Adsorption Capacities on Several Organic Adsorbents

adsorbent	adsorption capacity (mg/g)	references
organo-vermiculite (Na)	155	40
chitosan-coated sodium zeolites	287	41
zeolitic imidazolate framework	145	42
activated carbon from endemic *Vitis vinifera* L. grape seeds	79	43
Fe−La oxides co-loaded MgO nanosheets	39	44
N-acyl thiolated chitosan	435	45
reduced graphene oxide-hydroxyapatite hybrid composite	49	46
G_{16}-SiNPs	401	this study

3.3.4. Effect of Temperature and Adsorption Thermodynamics. MO adsorption exhibits a relative reverse trend with temperature (Figure 4d), verifying the exothermic nature during all MO adsorption processes. Thermodynamic parameters $\Delta H°$, $\Delta G°$, and $\Delta S°$ are calculated to test the thermodynamic characters.

Thermodynamic parameters could be calculated using the following equations:

$$\ln K_L = \frac{\Delta S°}{R} - \frac{\Delta H°}{RT} \quad (8)$$

$$\Delta G° = -RT \ln K_L \quad (9)$$

where K_L is the Langmuir constant and q_e and C_e have the same definitions as the above equations. R is the universal gas constant (8.3145 J/(mol K)) and T represents the absolute temperature in kelvin. The values of $\Delta H°$ and $\Delta S°$ can be extrapolated from intercept and slope of ln K_L versus $1/T$, respectively.

Negative values of $\Delta H°$ give evidence for the exothermic nature of MO adsorption (Table5). The negative values of $\Delta S°$

https://doi.org/10.1021/acsomega.1c01788
ACS Omega 2021, 6, 18014−18023

Table 5. Thermodynamic Parameters for MO on G_{16}-SiNPs

	ΔG° (kJ/mol)				
adsorbents	T = 298 K	T = 313 K	T = 328 K	ΔS° (J/(mol K))	ΔH° (kJ/mol)
G_{16}-SiNPs	6.28	9.02	11.76	−0.18	−48.12

reflect the decreases in randomness between the solid and solution interface. In addition, the positive ΔG° values suggest nonspontaneous adsorption processes. According to the literature that the physisorption energies are in the range of 0−20 kJ/mol, while the chemical sorption energies are between 80 and 400 kJ/mol,[47] it can be concluded that MO is physically adsorbed instead of chemical adsorption on G_{16}-SiNPs.

3.3.5. Effect of Solution pH. The variation of MO adsorption on G_{16}-SiNPs as a function of pH value is presented in Figure 5. The zeta potential of G_{16}-SiNPs continuously decreases with increasing pH, which, on the other hand, is always kept positive under all experimental conditions.

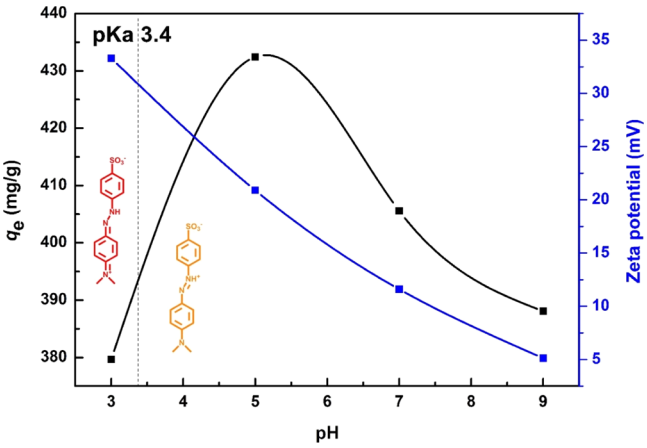

Figure 5. Effect of pH on MO adsorption and zeta potential values of G_{16}-SiNPs.

The important role of electrostatic interactions is verified from the effect of solution pH. As shown in Figure 5, the positive charge of G_{16}-SiNPs keeps decreasing but remains positive at all the tested pH values. With the solution pH varying from 3 to 5, the molecular form of MO molecules plays an important role for the variation of adsorption capacity. Reduced amounts of positively charged MO are beneficial for their electrostatic attractions with the surface of G_{16}-SiNPs, leading to the constantly increased adsorption trend. After the pH becomes higher than 5, the charge property of G_{16}-SiNPs dominates the adsorption trend (432.44, 405.58, and 388.08 mg/g corresponding to the pH of 5, 7, and 9, respectively). The decreased positive charge of G_{16}-SiNPs weakens the electrostatic interactions between the adsorbent and MO, indicating that the mainly controllable adsorption mechanism is not only electrostatic interactions but also the partition process and OH−π interactions (Figure 6).

Moreover, to further confirm the possible interactions between MO and G_{16}-SiNPs, the FT-IR spectra of MO and adsorbed MO/G16-SiNPs are recorded and presented in Figure S4.

Compared with G_{16}-SiNPs, additional peaks emerging between 1596 and 1380 cm^{-1} symbolize the aromatic rings of MO within the spectrum of MO/G_{16}-SiNPs.[48] The shift of

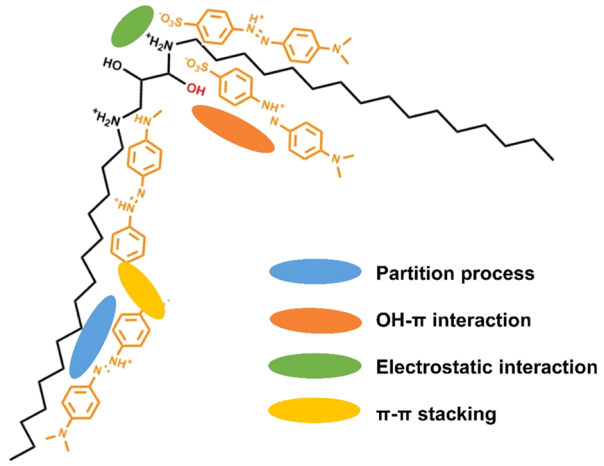

Figure 6. Schematic diagram of interactions between MO and G_{16}.

the −OH stretching vibration from 3391 to 3434 cm^{-1} indicates the existence of OH−π interactions. The existence of the partition process is proved by the shift of the $-CH_2$ bending vibration from 1468 to 1596 cm^{-1}.[49] Moreover, interactions between MO and the silica surface are verified by the variation of the Si−O peak (from 1097 to 1085 cm^{-1}).

3.4. Molecular Simulation and Computation. Understanding the adsorption mechanism of adsorbate molecules on the surface of the adsorbent is essential to explain the interaction between them and the optimal design of this type of adsorbent. In this section, the frontier orbital theory is used to obtain the optimal structure of MO and G_{16} and discuss their electronic orbital-related properties. All the optimized structures had been ensured that they were global minima through frequency calculations, and the results of frequency calculations are shown in the Supporting Information. The vibrational analysis data of the optimized structures of G_{16} and MO are presented in Table S2.

The optimized structures of MO, G_{16}, and their frontier orbitals have been given in Figure 7. Frontier orbitals include the HOMO and the LUMO. The electron on HOMO has the highest energy and is the least bound, so it is the most active and easy to change, while LUMO has the lowest energy among

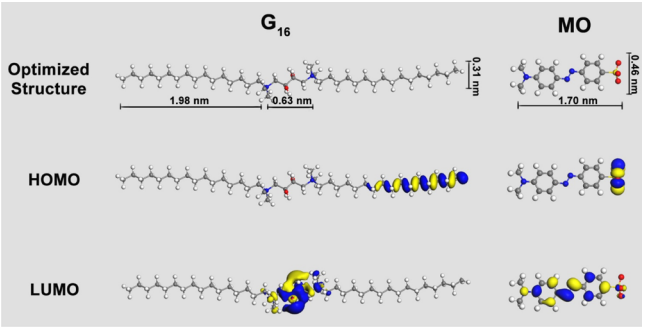

Figure 7. Optimized geometries, frontier molecular orbitals for the organic modifier, and MO calculated by DFT.

https://doi.org/10.1021/acsomega.1c01788
ACS Omega 2021, 6, 18014−18023

all unoccupied orbitals and is the easiest to accept electrons. Therefore, these two orbitals determine the electron gain or loss and transfer ability of the molecule, which determines important chemical properties such as the spatial orientation of intermolecular reactions. In addition to the orbital structure, the orbital energies (E_{HOMO} and E_{LUMO}) of two molecules are also given in Table 6.

Table 6. Frontier Orbital Energies of the Two Molecules

molecule	E_{HOMO} (eV)	E_{LUMO} (eV)
G_{16}	−4.465	−1.212
MO	−0.869	0.162

When two molecules interact with each other, the electrons in HOMOs and LUMOs would exchange. The energy difference between HOMO and LUMO determines the direction and strength of electron transfer. In Table 6, it is obvious that the energy difference between G_{16}-HOMO (−4.465 eV) and MO-LUMO (0.162 eV) is much greater than the energy difference between MO-HOMO (−0.869 eV) and G_{16}-LUMO (−1.212 eV). Therefore, electrons tend to transfer from MO to G_{16} during the adsorption process. It can be seen from Figure 7 that in the MO molecule, HOMO orbitals concentrate near the sulfur and oxygen atoms. For G_{16}, LUMO is concentrated in the central part. When G_{16} and MO interact during the adsorption process, the SO_3 group in MO will approach N atoms which are in the middle of G_{16} and exchange the electrons. This conclusion is also consistent with the positions of charged groups in the two molecules.

3.5. Desorption Tests. The regeneration performance of G_{16}-SiNPs is tested by ethanol. After three cycles, the MO adsorption decreases from 401.88 to 368.24, 354.06, and 350.98 mg/g, evidencing the considerable adsorption active sites within G16-SiNPs. Although the original adsorption sites are partially occupied due to adsorption and/or desorption, there are still new binding sites emerging on the adsorbent surface, accounting for the stability during regeneration processes.[50]

4. CONCLUSIONS

A novel multi-hydroxyl-containing gemini surfactant (G_{16}) is first designed for modification of emerging SiNPs for fabricating an organic adsorbent targeted at MO. The resultant G_{16}-SiNPs exhibit enhanced hydrophobicity, enlarged interlayer spacing, and increased thermal weight losses. The immobilization strength of G_{16} on SiNPs is ordered in the sequence of electrostatic interactions > physical adsorption > van der Waals forces, with the combination of which contributing to the unprecedented high modifier availability (approximately 100%).

Effective MO adsorption is obtained from the comparison between SiNPs (64.72 mg/g) and G_{16}-SiNPs (401.88 mg/g), which is higher than those of most of the existing silica-based adsorbents. Pseudo-second-order and Langmuir models conform to all adsorption processes, indicating that the adsorption rate mainly relies on the availability of adsorption sites and is characterized by a homogeneous adsorption form. Thermodynamic parameters show the nonspontaneous and exothermic nature of the adsorption process. By combining the results of adsorption kinetics, isotherms, thermodynamics, and frontier molecular orbitals, the as-synthesized adsorbent G_{16}-SiNPs own diverse active sites that contribute to multi-adsorption mechanisms: the partition process (derived from the alkyl chain of G_{16}), electrostatic interactions (derived from the N^+ head group of G_{16}), and OH−π interactions (derived from the hydroxyl group of G_{16}), contributing to the excellent adsorption performance of G_{16}-SiNPs. It can be concluded that G_{16}-SiNPs are a synergistic, efficient, and promising adsorbent for removing anionic dyes from contaminated water.

■ ASSOCIATED CONTENT

Supporting Information

The Supporting Information is available free of charge at https://pubs.acs.org/doi/10.1021/acsomega.1c01788.

Characterization operations, equations about adsorption kinetics, isotherms, and thermodynamics (PDF)

■ AUTHOR INFORMATION

Corresponding Authors

Shifeng Wang − *Department of Physics, Innovation Center of Materials for Energy and Environment Technologies, College of Science and Institute of Oxygen Supply, Center of Tibetan Studies (Everest Research Institute), Tibet University, Lhasa 850000, China; Key Laboratory of Cosmic Rays, Ministry of Education, Tibet University, Lhasa 850000, China;* orcid.org/0000-0001-6169-2598; Email: wsf@utibet.edu.cn

Qi Gao − *Department of Physics, Innovation Center of Materials for Energy and Environment Technologies, College of Science, Tibet University, Lhasa 850000, China; Key Laboratory of Cosmic Rays, Ministry of Education, Tibet University, Lhasa 850000, China*; Email: fbc1980@163.com

Authors

Tingting Wang − *Department of Physics, Innovation Center of Materials for Energy and Environment Technologies, College of Science and Institute of Oxygen Supply, Center of Tibetan Studies (Everest Research Institute), Tibet University, Lhasa 850000, China; Key Laboratory of Cosmic Rays, Ministry of Education, Tibet University, Lhasa 850000, China; Hoffmann Institute of Advanced Materials, Shenzhen Polytechnic, Shenzhen 518055, P. R. China*

Yaxun Sun − *Department of Physics, Innovation Center of Materials for Energy and Environment Technologies, College of Science and Institute of Oxygen Supply, Center of Tibetan Studies (Everest Research Institute), Tibet University, Lhasa 850000, China; Key Laboratory of Cosmic Rays, Ministry of Education, Tibet University, Lhasa 850000, China*

Xin Li − *Department of Physics, Innovation Center of Materials for Energy and Environment Technologies, College of Science and Institute of Oxygen Supply, Center of Tibetan Studies (Everest Research Institute), Tibet University, Lhasa 850000, China; Key Laboratory of Cosmic Rays, Ministry of Education, Tibet University, Lhasa 850000, China; Hoffmann Institute of Advanced Materials, Shenzhen Polytechnic, Shenzhen 518055, P. R. China*

Yihang Yue − *Department of Physics, Innovation Center of Materials for Energy and Environment Technologies, College of Science and Institute of Oxygen Supply, Center of Tibetan Studies (Everest Research Institute), Tibet University, Lhasa 850000, China; Key Laboratory of Cosmic Rays, Ministry of Education, Tibet University, Lhasa 850000, China*

Complete contact information is available at:

https://doi.org/10.1021/acsomega.1c01788
ACS Omega 2021, 6, 18014−18023

https://pubs.acs.org/10.1021/acsomega.1c01788

Author Contributions

⊥T.W. and Y.S. contributed equally in this work.

Notes

The authors declare no competing financial interest.

■ ACKNOWLEDGMENTS

This research was funded by the National Natural Science Foundation of China (nos: 52062045, 12047575, and 11765019), the Central Government Funds for the Reform and Development of Local Colleges and Universities (no: ZCKJ 2020-11), the Central Government Funds for Local Scientific and Technological Development (no.: XZ202101YD0019C), and the Everest Discipline Construction Project of Tibet University (no.: ZF21000002).

■ REFERENCES

(1) Azha, S. F.; Shamsudin, M. S.; Shahadat, M.; Ismail, S. Low cost zwitterionic adsorbent coating for treatment of anionic and cationic dyes. *J. Ind. Eng. Chem.* **2018**, *67*, 187−198.
(2) Wang, H.; Chen, Z.; Chen, D.; Yu, Q.; Yang, W.; Zhou, J.; Wu, S. Facile, template-free synthesis of macroporous SiO_2 as catalyst support towards highly enhanced catalytic performance for soot combustion. *Chem. Eng. J.* **2019**, *375*, 121958.
(3) Zhou, Y.; Lu, J.; Zhou, Y.; Liu, Y. Recent advances for dyes removal using novel adsorbents: A review. *Environ. Pollut.* **2019**, *252*, 352−365.
(4) Maheria, K. C.; Chudasama, U. V. Sorptive Removal of Dyes Using Titanium Phosphate. *Ind. Eng. Chem. Res.* **2007**, *46*, 6852−6857.
(5) Ferreira, T. A.; Ibarra, I. S.; Silva, M. L. S.; Miranda, J. M.; Rodriguez, J. A. Use of modified henequen fibers for the analysis of malachite green and leuco-malachite green in fish muscle by d-SPE followed by capillary electrophoresis. *Microchem. J.* **2020**, *157*, 104941.
(6) Madrakian, T.; Afkhami, A.; Ahmadi, M.; Bagheri, H. Removal of some cationic dyes from aqueous solutions using magnetic-modified multi-walled carbon nanotubes. *J. Hazard. Mater.* **2011**, *196*, 109−114.
(7) Kausar, A.; Iqbal, M.; Javed, A.; Aftab, K.; Nazli, Z.-i. -H.; Bhatti, H. N.; Nouren, S. Dyes adsorption using clay and modified clay: A review. *J. Mol. Liq.* **2018**, *256*, 395−407.
(8) Yu, X.; Wei, C.; Ke, L.; Hu, Y.; Xie, X.; Wu, H. Development of organovermiculite-based adsorbent for removing anionic dye from aqueous solution. *J. Hazard. Mater.* **2010**, *180*, 499−507.
(9) Khalil, M.; Amanda, A.; Yunarti, R. T.; Jan, B. M.; Irawan, S. Synthesis and application of mesoporous silica nanoparticles as gas migration control additive in oil and gas cement. *J. Petrol. Sci. Eng.* **2020**, *195*, 107660.
(10) Ryu, J.; Hong, D.; Choi, S.; Park, S. Synthesis of Ultrathin Si Nanosheets from Natural Clays for Lithium-Ion Battery Anodes. *ACS Nano* **2016**, *10*, 2843−2851.
(11) Trouvé, A.; Batonneau-Gener, I.; Valange, S.; Bonne, M.; Mignard, S. Tuning the hydrophobicity of mesoporous silica materials for the adsorption of organic pollutant in aqueous solution. *J. Hazard. Mater.* **2012**, *201−202*, 107−114.
(12) Shen, T.; Mao, S.; Ding, F.; Han, T.; Gao, M. Selective adsorption of cationic/anionic tritoluene dyes on functionalized amorphous silica: A mechanistic correlation between the precursor, modifier and adsorbate. *Colloids Surf., A* **2021**, *618*, 126435.
(13) Park, Y.; Ayoko, G. A.; Frost, R. L. Application of organoclays for the adsorption of recalcitrant organic molecules from aqueous media. *J. Colloid Interface Sci.* **2011**, *354*, 292−305.
(14) Xiang, Y.; Gao, M.; Shen, T.; Cao, G.; Zhao, B.; Guo, S. Comparative study of three novel organo-clays modified with imidazolium-based gemini surfactant on adsorption for bromophenol blue. *J. Mol. Liq.* **2019**, *286*, 110928.
(15) Kaczerewska, O.; Brycki, B.; Ribosa, I.; Comelles, F.; Garcia, M. T. Cationic gemini surfactants containing an O-substituted spacer and hydroxyethyl moiety in the polar heads: Self-assembly, biodegradability and aquatic toxicity. *J. Ind. Eng. Chem.* **2018**, *59*, 141−148.
(16) Shen, T.; Gao, M. Gemini surfactant modified organo-clays for removal of organic pollutants from water: A review. *Chem. Eng. J.* **2019**, *375*, 121910.
(17) Wang, J.; Gao, M.; Shen, T.; Yu, M.; Xiang, Y.; Liu, J. Insights into the efficient adsorption of rhodamine B on tunable organo-vermiculites. *J. Hazard. Mater.* **2019**, *366*, 501−511.
(18) Vaupel, S.; Brutschy, B.; Tarakeshwar, P.; Kim, K. S. Characterization of Weak NH−π Intermolecular Interactions of Ammonia with Various Substituted π-Systems. *J. Am. Chem. Soc.* **2006**, *128*, 5416−5426.
(19) Stojanović, S. Đ.; Medaković, V. B.; Predović, G.; Beljanski, M.; Zarić, S. D. XH/π interactions with the π system of porphyrin ring in porphyrin-containing proteins. *JBIC, J. Biol. Inorg. Chem.* **2007**, *12*, 1063−1071.
(20) Shen, T.; Wang, L.; Zhao, Q.; Guo, S.; Gao, M. Single and simultaneous adsorption of basic dyes by novel organo-vermiculite: A combined experimental and theoretical study. *Colloids Surf., A* **2020**, *601*, 125059.
(21) Lawal, I. A.; Lawal, M. M.; Azeez, M. A.; Ndungu, P. Theoretical and experimental adsorption studies of phenol and crystal violet dye on carbon nanotube functionalized with deep eutectic solvent. *J. Mol. Liq.* **2019**, *288*, 110895.
(22) Han, T.; Guo, J.; Zhao, Q.; Wu, Y.; Zhang, Y. Enhanced corrosion inhibition of carbon steel by pyridyl gemini surfactants with different alkyl chains. *Mater. Chem. Phys.* **2020**, *240*, 122156.
(23) Ren, L.; Cheng, Y.; Shao, R.; Meng, X.; Yang, J.; Wang, Q. DFT studies of adsorption properties and bond strengths of H2S, HCN and NH3 on Fe(1 0 0). *Appl. Surf. Sci.* **2020**, *500*, 144232.
(24) Yu, X.-b.; Wei, C.-h.; Ke, L.; Wu, H.-z.; Chai, X.-s.; Hu, Y. Preparation of trimethylchlorosilane-modified acid vermiculites for removing diethyl phthalate from water. *J. Colloid Interface Sci.* **2012**, *369*, 344−351.
(25) Zhao, M.; Tang, Z.; Liu, P. Removal of methylene blue from aqueous solution with silica nano-sheets derived from vermiculite. *J. Hazard. Mater.* **2008**, *158*, 43−51.
(26) Hanaoka, T.; Arao, Y.; Kayaki, Y.; Kuwata, S.; Kubouchi, M. Analysis of nitric acid decomposition of epoxy resin network structures for chemical recycling. *Polym. Degrad. Stab.* **2021**, *186*, 109537.
(27) Yang, Q.; Gao, M.; Luo, Z.; Yang, S. Enhanced removal of bisphenol A from aqueous solution by organo-montmorillonites modified with novel Gemini pyridinium surfactants containing long alkyl chain. *Chem. Eng. J.* **2016**, *285*, 27−38.
(28) Chen, B.; Zhu, L.; Zhu, J.; Xing, B. Configurations of the Bentonite-Sorbed Myristylpyridinium Cation and Their Influences on the Uptake of Organic Compounds. *Environ. Sci. Technol.* **2005**, *39*, 6093−6100.
(29) Nickels, T. M.; Ingram, A. L.; Maraoulaite, D. K.; White, R. L. Thermogravimetry-mass spectrometry investigations of benzoic acid interactions with sodium and calcium montmorillonites. *Thermochim. Acta* **2015**, *614*, 157−162.
(30) Mueller, R.; Kammler, H. K.; Wegner, K.; Pratsinis, S. E. OH surface density of SiO_2 and TiO_2 by thermogravimetric analysis. *Langmuir* **2003**, *19*, 160−165.
(31) Cheng, Z.; Shan, H.; Sun, Y.; Zhang, L.; Jiang, H.; Li, C. Evolution mechanism of surface hydroxyl groups of silica during heat treatment. *Appl. Surf. Sci.* **2020**, *513*, 145766.
(32) Abdallah, W.; Yilmazer, U. Novel thermally stable organo-montmorillonites from phosphonium and imidazolium surfactants. *Thermochim. Acta* **2011**, *525*, 129−140.
(33) Rytwo, G.; Nir, S.; Margulies, L. Interactions of Monovalent Organic Cations with Montmorillonite: Adsorption Studies and Model Calculations. *Soil Sci. Soc. Am. J.* **1995**, *59*, 554−564.

(34) Xue, G.; Gao, M.; Gu, Z.; Luo, Z.; Hu, Z. The removal of p-nitrophenol from aqueous solutions by adsorption using gemini surfactants modified montmorillonites. *Chem. Eng. J.* **2013**, *218*, 223−231.
(35) Yang, S.; Gao, M.; Luo, Z. Adsorption of 2-Naphthol on the organo-montmorillonites modified by Gemini surfactants with different spacers. *Chem. Eng. J.* **2014**, *256*, 39−50.
(36) Wu, F.-C.; Tseng, R.-L.; Huang, S.-C.; Juang, R.-S. Characteristics of pseudo-second-order kinetic model for liquid-phase adsorption: A mini-review. *Chem. Eng. J.* **2009**, *151*, 1−9.
(37) Yang, S.; Gao, M.; Luo, Z.; Yang, Q. The characterization of organo-montmorillonite modified with a novel aromatic-containing gemini surfactant and its comparative adsorption for 2-naphthol and phenol. *Chem. Eng. J.* **2015**, *268*, 125−134.
(38) Guo, X.; Wang, J. Comparison of linearization methods for modeling the Langmuir adsorption isotherm. *J. Mol. Liq.* **2019**, *296*, 111850.
(39) Janiak, C. A critical account on $\pi-\pi$ stacking in metal complexes with aromatic nitrogen-containing ligands. *J. Chem. Soc., Dalton Trans.* **2000**, 3885−3896.
(40) Zang, W.; Gao, M.; Shen, T.; Ding, F.; Wang, J. Facile modification of homoionic-vermiculites by a gemini surfactant: Comparative adsorption exemplified by methyl orange. *Colloids Surf., A* **2017**, *533*, 99−108.
(41) Hussain, S.; Kamran, M.; Khan, S. A.; Shaheen, K.; Shah, Z.; Suo, H.; Khan, Q.; Shah, A. B.; Rehman, W. U.; Al-Ghamdi, Y. O.; Ghani, U. Adsorption, kinetics and thermodynamics studies of methyl orange dye sequestration through chitosan composites films. *Int. J. Biol. Macromol.* **2021**, *168*, 383−394.
(42) Ba Mohammed, B.; Lgaz, H.; Alrashdi, A. A.; Yamni, K.; Tijani, N.; Dehmani, Y.; El Hamdani, H. Insights into methyl orange adsorption behavior on a cadmium zeolitic-imidazolate framework Cd-ZIF-8: A joint experimental and theoretical study. *Arabian J. Chem.* **2021**, *14*, 102897.
(43) Yönten, V.; Sanyürek, N. K.; Kivanç, M. R. A thermodynamic and kinetic approach to adsorption of methyl orange from aqueous solution using a low cost activated carbon prepared from Vitis vinifera L. *Surf. Interfaces* **2020**, *20*, 100529.
(44) Sun, X.; Zhou, Y.; Zheng, X. Comparison of adsorption behaviors of Fe-La oxides co-loaded MgO nanosheets for the removal of methyl orange and phosphate in single and binary systems. *J. Environ. Chem. Eng.* **2020**, *8*, 104252.
(45) Borsagli, F. G. L. M.; Ciminelli, V. S. T.; Ladeira, C. L.; Haas, D. J.; Lage, A. P.; Mansur, H. S. Multi- functional eco-friendly 3D scaffolds based on N-acyl thiolated chitosan for potential adsorption of methyl orange and antibacterial activity against Pseudomonas aeruginosa. *J. Environ. Chem. Eng.* **2019**, *7*, 103286.
(46) Karthikeyan, P.; Elanchezhiyan, S. S. D.; Banu, H. A. T.; Hasmath Farzana, M.; Park, C. M. Hydrothermal synthesis of hydroxyapatite-reduced graphene oxide (1D−2D) hybrids with enhanced selective adsorption properties for methyl orange and hexavalent chromium from aqueous solutions. *Chemosphere* **2021**, *276*, 130200.
(47) Rytwo, G.; Ruiz-Hitzky, E. Enthalpies of adsorption of methylene blue and crystal violet to montmorillonite. *J. Therm. Anal. Calorim.* **2003**, *71*, 751−759.
(48) Rytwo, G.; Nir, S.; Margulies, L. Interactions of monovalent organic cations with montmorillonite: Adsorption studies and model calculations. *Soil Sci. Soc. Am. J.* **1995**, *59*, 554−564.
(49) Oki, M.; Iwamura, H. Steric effects on the O-Hπ interaction in 2-hydroxybiphenyl. *J. Am. Chem. Soc.* **1967**, *89*, 576−579.
(50) Stawiński, W.; Węgrzyn, A.; Freitas, O.; Chmielarz, L.; Mordarski, G.; Figueiredo, S. Simultaneous removal of dyes and metal cations using an acid, acid-base and base modified vermiculite as a sustainable and recyclable adsorbent. *Sci. Total Environ.* **2017**, *576*, 398−408.

https://doi.org/10.1021/acsomega.1c01788
ACS Omega 2021, 6, 18014−18023